10

Prototype UWB Radar Object Scanner and Holographic Signal Processing

**Lorenzo Capineri, Timothy Bechtel, Pierluigi Falorni,
Masaharu Inagaki, Sergey Ivashov, and Colin Windsor**

CONTENTS

10.1 Introduction

Subsurface imaging using high-frequency impulse ground-penetrating radar has long been studied and applied in fields such as geotechnical, environmental, and structural engineering [1]. More recently ultrawideband (UWB) radar technology has stimulated new investigations into aerospace and medical (among others) applications [2]. However, it is a common problem that the detection of shallow targets (depth < 20 cm) is hindered by interference between the transmitted and received pulses from shallow electromagnetic impedance contrasts. Mitigating these interference effects requires complex methods of image reconstruction. The authors developed a different approach to short-range materials penetrating radar using holographic radar, which measures the phase of the reflected signal. Demonstration

holographic radars operating at 2 GHz and 4 GHz can produce useful images with high spatial resolution over a variety of subsurface impedance contrasts [3,4,5]. However, both impulse and holographic high-frequency radars are commonly limited to scanning small areas on the order of 1 or 2 m² using manual scanning [6]. This time-consuming data acquisition method requires the preparation of a grid of reference lines on the scanned surface to guide the manual operation. Deviations from the guiding lines are common, and it is difficult to maintain accurate location control for larger areas (e.g., several square meters). Moreover, the trend toward using higher frequencies (>4 GHz) in subsurface imaging is sustained by the availability of integrated electronic devices operating in this frequency range with improved power consumption and signal-to-noise ratio, and with high-resolution analog-to-digital converters. The shorter wavelength can improve the spatial resolution of phase-based images, but only if a comparable sample step (a few millimeters) is employed and the uncertainty of manual scanning is also limited to a few millimeters. Free-hand scans are possible indoors or outdoors with advanced optical, pulsed microwave, or ultrasonic positioning systems [7,8,9] having millimeter accuracy, but the acquisition rate is slow compared with manual scanning. In addition, set up time and environmental conditions such as natural or artificial light, electromagnetic interference, or air turbulence can limit their applicability. Finally, the cost of the instruments and their set up time is another limiting factor.

A new approach, proposed recently [10,11,12], is the development of a light, compact, robotic holographic radar scanner capable of imaging large areas with fine spatial sampling. The holographic radar was developed with a compact and lightweight (<400 g) monostatic antenna with integrated electronics swept by a mechanical scanner mounted on a robotic vehicle. The trajectory of the robotic vehicle is programmable from a remote PC terminal in order to cover arbitrary areas while avoiding obstacles. The holographic images have a plan-view resolution that is about a quarter of the signal wavelength in the scanned material (e.g., soil, stone, and wood), and they accurately reproduce the dimensions and shape of shallow objects with a contrasting dielectric constant. A full three-dimensional reconstruction containing depth information can be obtained using multiple frequencies and migration software [13].

In addition to the radar itself, the newly available fast developing robotic technologies for the platform/positioning can simplify the design of the mechanics, the electronics, and the trajectory control. This has motivated research into a prototype robotic scanner that combines the benefits of high-spatial-resolution subsurface radar imaging and the automated robotic scanning of indoor or outdoor surveys.

In this chapter, Section 10.2 reviews the underlying theory of the sampling requirements for subsurface imaging with holographic radar. Section 10.3 presents the applicable holographic signal-processing techniques. Section 10.4 describes the principles of operation for the robotic scanner prototype and the laboratory implementation of a high-accuracy automated scanner. Finally, Section 10.5 illustrates investigations in several fields using this subsurface imaging method and emphasizes the real benefits of this robotic approach to high-frequency GPR scanning relative to the standard manual scanning.

10.2 Holographic Subsurface Radars of the RASCAN Type

10.2.1 Principles of Radar Holography

The holographic subsurface radar design uses the classical principles of radio-positioning. As in all radar, the radiated signal reflects from local inhomogeneities if their dielectric

constant ε differs from the surrounding medium dielectric constant. The receiving antenna collects the reflected signal. The receiver amplifies and registers the reflected signal. After appropriate signal processing, the operator sees the results displayed on a computer screen in real time [see, e.g., 14].

Traditionally, impulse radar is the most commonly used type of subsurface radar. In general, these repeatedly transmit a single period of a sine wave signal (or impulse), and record the time-domain return signal (or wiggle trace), which contains the reflected impulses. Currently, almost all subsurface radars in commercial production are of this type. The main advantage of impulse radar is the high-effective penetration depth into the surveyed medium achieved by application of time-varying gain, which amplifies the later weaker signals from deeper reflections. A direct determination of reflector depths may be made by measurement of the reflected signal time-of-flight if the electromagnetic wave velocity in the medium is known or determinable [14,15]. Impulse radars have a significant disadvantage from the reverberation effect, that is multiple reflections of the transmitted pulse between the radar antenna and strong reflectors (such as the metal supporting structure to which thermal insulation or heat protection coatings are attached – see Section 10.5). In this case, multiple reflections (often called ghosts or phantoms) of the transmitted impulse signal obscure the primary reflection of interest [16].

RASCAN-type holographic subsurface radars are free from this reverberation effect because they use a continuous wave signal. RASCAN radars also have a distinct advantage in lateral resolution over impulse radars because of the specific design of the radar antenna which combines the transmitter and receiver antennas into one lightweight and compact apparatus with a small footprint.

Holographic subsurface radars get their name from the process of recording the interference pattern on the surface of the medium between the reference wave and the wave (object wave) reflected from subsurface targets. It is worth noting that for a long time, there was a widespread opinion that, due to strong attenuation in typical media and the inapplicability of time-varying gain to continuous wave radar reflections, holographic subsurface radar was unlikely to find any significant practical application [17]. However, the recent development of holographic subsurface radar of the RASCAN type, their commercial production, and sufficiently broad practical application have shown that for examination of low electrical conductivity media at shallow depths, this type of device has many advantages including real-time, plan-view imaging, and high lateral resolution. The design details of the various types of RASCAN radar and their areas of application are described in [18,19] and [3,5].

The principles of recording microwave holograms using RASCAN radar are analogous to optical holography. Consider a plane monochromatic wave with a constant phase (the reference wave) encountering a point target and scattering. The summation of the incident (or reference) and scattered (or object) waves on a flat screen located at some distance behind the object forms an interference pattern as in Figure 10.1a. If the screen is normal to the propagation direction of the reference wave, the interference pattern forms a Fresnel pattern of concentric rings. In optics, after development of the pattern recorded on a photographic plate, illuminating the pattern by a reference wave will form a virtual image of the object, which seems to float behind the screen as in Figure 10.1b. A similar phenomenon occurs when a RASCAN subsurface holographic radar records a microwave hologram of a point target in a uniform medium [13].

In some cases, microwave holograms recorded by RASCAN are remarkably similar to the optical holograms shown in the classical work of D. Gabor [20]. The essential difference is the much lower spatial density of interference lines on the microwave hologram
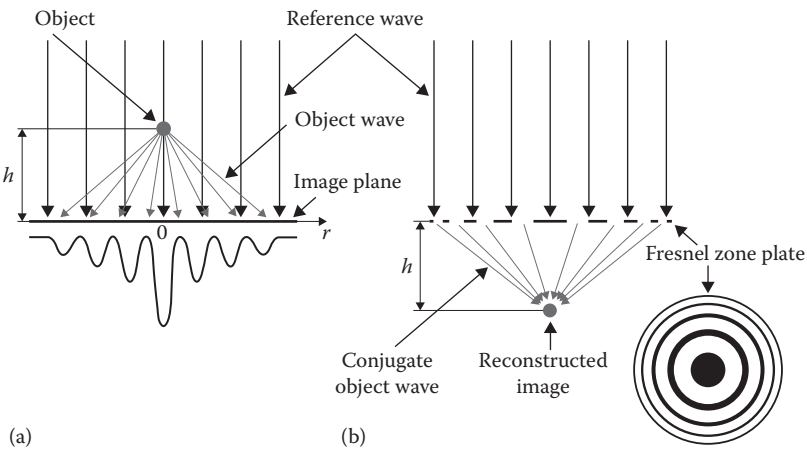
FIGURE 10.1
The holographic radar uses the same principles as an optical hologram. (a) The simplest case of recording of the holographic diffraction pattern for a point target and (b) reconstruction of the target image using the diffraction pattern.

interference patterns [21]. This is because at approximately the same characteristic dimensions of the systems, the radar wavelength is several orders of magnitude greater than wavelengths in the optical waveband.

RASCAN radars have fully implemented this holographic principle. Figure 10.2 shows the subsurface radar RASCAN-5/15000 used in some of the experiments described in this chapter. Radars of RASCAN-5 type use a quadrature signal receiver that allows recording of complex microwave holograms of hidden objects. The radar transducer head containing both a transmitter and a receiver connects via a network cable to a microcontroller unit through a USB link to a computer. The microcontroller unit drives the transmitter and receiver, digitizes the received data, and transmits it to the computer.

Image formation using holographic radar results from scanning a surface using a monostatic antenna. The defined antenna position (x, y) over this surface assumes an ideal planar surface. Computation assumes a reference system (x, y, and z) with the origin on this surface and the perpendicular z-axis representing the depth (Figure 10.3).

FIGURE 10.2
The holographic subsurface radar RASCAN-5/15000 as supplied to customers. The wheel on the radar transducer head measures movement of the radar during scanning.
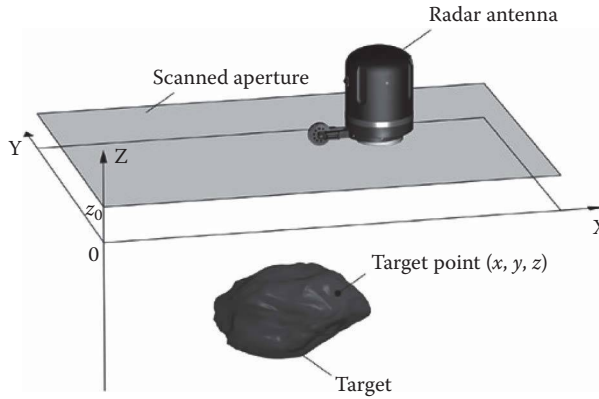
FIGURE 10.3
Geometry of holographic imaging system with a RASCAN head.

Single-frequency holographic image reconstruction used the following set of basic equations:

$$F(k_x, k_y) = \frac{1}{(2\pi)^2} \iint E(x,y) e^{-i(k_x x + k_y y)} dx dy \tag{10.1}$$

$$S(k_x, k_y, z) = F(k_x, k_y) e^{i\sqrt{4(\omega\sqrt{\varepsilon}/c)^2 - k_x^2 - k_y^2} \cdot (z_0 - z)} \tag{10.2}$$

$$E_R(x, y, z) = \iint S(k_x, k_y, z) e^{i(k_x x + k_y y)} dk_x dk_y \tag{10.3}$$

where:
  $F(x,y)$ is the plane wave decomposition of the complex conjugate to hologram $E(x, y, z)$
      registered at the interface $z = 0$.
  $S(k_x, k_y, z)$ expresses the propagation of this pattern back to the focusing plane.
  $E_r(x, y, z)$ is the reconstructed image.
  ω is the temporal angular frequency.
  ε is the dielectric permittivity of the medium.
  c is the speed of light.
  k_x and k_y are the spatial frequencies corresponding to the x and y dimensions, respectively.

10.2.2 Spatial and Frequency Sampling Requirements

Generally, the holographic radar assumes a homogeneous scanned medium with a constant propagation velocity v. Implementing the mathematical integral formulation in Equations 10.1, 10.2, and 10.3 requires considering continuous spatial sampling at a discrete grid of points. The imaging process defines the spatial sampling according to the well-known Nyquist criterion. The Nyquist criterion is satisfied if the phase shift from one sample point to the next is less than π radians. For a spatial sample interval of Δx, the worst case will have a phase shift of not more than $2k_x \Delta x$, with similar formulation along the y coordinate. Therefore, the derived spatial sampling criterion for shallow objects is as follows:

$$\Delta x < \frac{\lambda}{4}; \ \Delta y < \frac{\lambda}{4} \tag{10.4}$$

TABLE 10.1

Holographic Radar Characteristics and Sampling Requirement

| Parameter	Rascan-4/2000	Rascan-4/4000	Rascan-4/7000
Frequency range, GHz	1.6–2.0	3.6–4.0	6.4–6.8
Number of operating frequencies		5	
Number of recording signal polarizations		2	
Resolution in the plane of sounding at shallow depths, cm	4	2	1–5
Maximal sounding depth R_{max} (depends on medium permittivity), cm	35	20	15
Spatial sampling $\Delta x < \lambda_c/4$; $\Delta y < \lambda_c/4$ (hp: $v = c/\sqrt{\varepsilon} = c/3 = 10^8 \text{m/s}$), cm	<1.3	<0.65	<0.38
Frequency sampling $\Delta f < v/(4R_{max})$, MHZ	71	125	166

where:

$\lambda = 2\pi/k$ is the wavelength

k is the spatial frequency

The frequency sampling requires that $2\Delta k\, R_{max} < \pi$, where R_{max} is the maximum target range, which means $\Delta f < c/(4R_{max})$. Table 10.1 presents the sampling requirements for three different models of RASCAN holographic radar. We can observe that the spatial sampling has to be done in steps less than 13 mm for the lower frequency and 3.8 mm for the highest frequency. It is straightforward that the high-resolution capability can only be achieved if the spatial sampling has a precision much better than these limits. The manual scanning method is intrinsically prone to errors and it is hard to reach these requirements even with skilled operators. Moreover, the acquisition of data from large areas involves a time-consuming process with consequences for the cost of the survey.

10.3 Holographic Radar and Electronic Signal Processing

The detection of a target by holographic radar relies on the complex reflection coefficient of the target and also the distance from the monostatic transmitter-receiver (see Figure 10.1). The measurement of the phase and magnitude (or I and Q components) of the received signals is necessary to allow a complete holographic reconstruction of subsurface targets. The acquisition of both I and Q components has been implemented in a recent version of the holographic radar that can also operate at higher frequency (7 GHz) than previous versions. The block scheme of the hardware is shown in Figure 10.4.

To maintain compatibility with earlier versions, the first version of this system achieved manual scan positioning using a wheel and optical encoder with the scan started by pressing a button on the bottom left of the transducer in Figure 10.2. The present version has enhanced versatility by programming an interface with a PC through a USB port, which allows automated collection of precisely located I/Q data for processing into a full 3D holographic reconstruction.
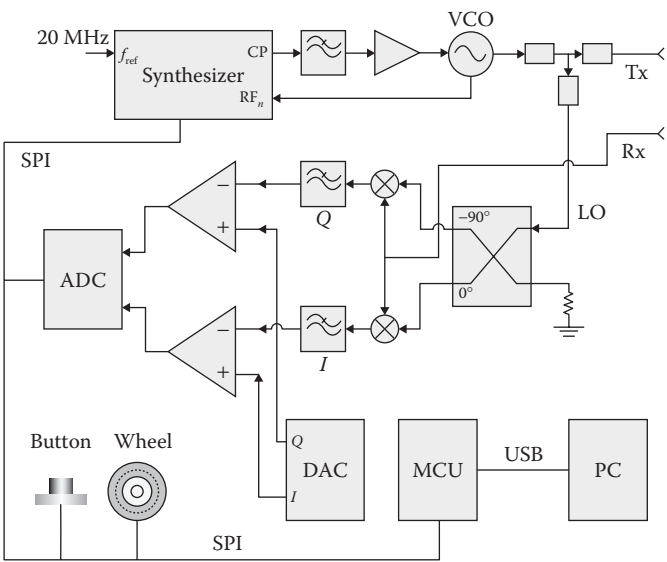
FIGURE 10.4
Block diagram of the electronic system for I/Q component acquisition with holographic radar.

10.4 Practical Scanning Methods and Trade-Offs

10.4.1 Scanner Design Objectives and Constraints

The scanning of large areas (several square meters) is of particular importance for inspecting civil engineering structures such as floors, pavements, and corridors; for minimum metal antipersonnel landmine detection; and shallow imaging of archaeological sites. Even the inspection of smaller areas as in the nondestructive testing (NDT) of engineering materials or of historic artworks or architectural elements requires scanning methods that must ensure adequate speed with high resolution and accuracy. The spatial accuracy is very important in holographic radar imaging because the phase coherence must be preserved in order to reconstruct the full hologram.

In the laboratory, it is possible to design accurate mechanical scanning systems with submillimeter accuracy and millimeter resolution that are adequate for preserving signal coherence. Moreover, the cost of such systems is prohibitive and limits the scanner applicability to areas with typical size of about a square meter. Generally, 2D scanners work best to spatially sample flat surfaces. For 3D surfaces, alternate solutions include mounting the radar head on an articulated robotic arm.

In outdoor environments, the proposed solution is a robotic platform that guarantees sufficient accuracy in the spatial sampling and requires little set up time. In our robotic platform, the antenna moves laterally (across-track) with a mechanical scanner, whereas the entire system moves (along-track) using four wheels with encoders attached to the axes of brush-less DC motors. This robotic configuration is implemented in a proof-of-concept prototype.

10.4.2 Robot Object Scanner (ROS) Design and Realization

Figure 10.5 shows the block diagram of the prototype robotic scanner. The open architecture allows the connection of different electronic units (custom or commercial) interfaced by an RS485 bus. This standard bus is simple to manage and robust for connections with low data rate as in the case of this application. In Figure 10.5, there are three main units as follows:

1. Communication and master control board
2. Movement control system
3. Lateral scanning control system

The Communication and master control board has eight analog input channels, eight analog output channels, and an I/O digital port based on the PIC18F6722 (microchip) microcontroller. This board allows the transmission of commands to other electronic units and reception of data by interrupt or polling methods. It also establishes remote communication using a Bluetooth version 3 protocol. This board acquires the position of the driving wheels connected to DC motors from the Movement Control Board, and the lateral position of the scanner at the front of the robotic platform as shown in Figure 10.5. The board acquires simultaneously the positioning data, the horizontal and cross polarization data from the two holographic radar channels demodulated at low frequency (up to 2 kHz bandwidth), and the tri-axial accelerometer and the scanner height from
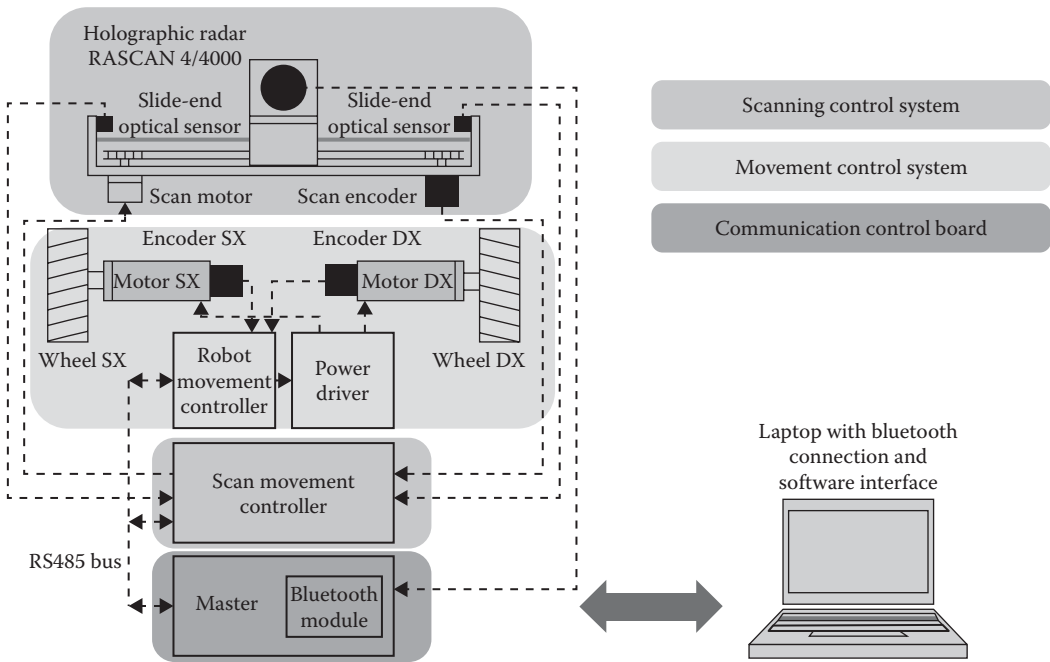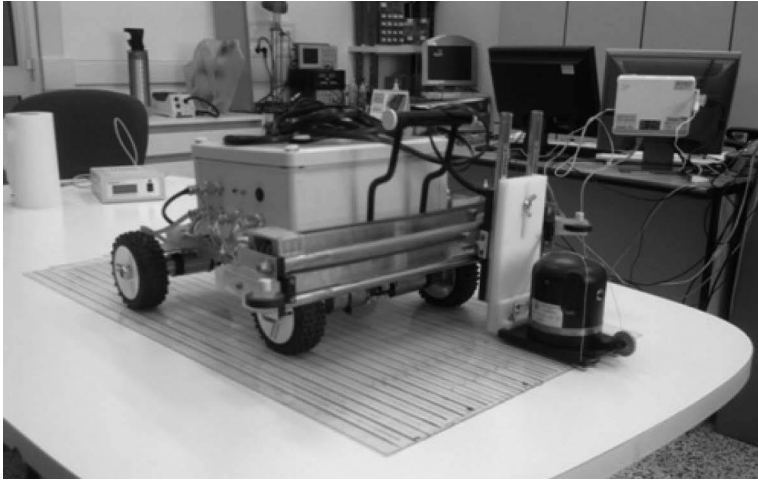

FIGURE 10.5
Block scheme of the robotic platform with interface for holographic radar and other sensors.

FIGURE 10.6
Lateral mechanical movement (along *y*) of the holographic radar head (RASCAN-4/4000) mounted on the robotic scanner. The electronics unit is mounted in a sealed PVC box with connectors for external battery, motors, and sensors.

the ultrasonic channel [22]. The movement electronic unit calculates the assigned trajectory (linear, piecewise linear, or circular) and minimizes the positioning errors with a Lyapunov controller. Similarly, the lateral scanner provides position control of the radar head, covering a swath about 28 cm wide. For each acquired position, all the information is packed into a custom frame structure and sent via the serial protocol to the remote PC (Figure 10.6).

Because the electromagnetic properties of the environment can change in time and space, the robotic system design can host multiple sensors, which allows different data to be spatially correlated. The signal processing of this information can enhance the detectability, positioning, and characterization of shallow targets. Essentially, the robotic platform has been developed in an open manner, with the option of using additional sensors, in addition to the more advanced versions of holographic radar with I/Q output channels, as previously described.

A possible set of single-point sensors useful for mapping environment parameters are as follows:

1. Metal detector for discriminating metallic versus nonmetallic targets imaged by radar.
2. Low-frequency ultrasonic transducers for ranging the air gap between the antenna and soil: this information is necessary to correct the disturbance (phase shift) effects on the holographic radar image.
3. Noncontact sensors for soil temperature: high-sensitivity pyroelectric or silicon sensors can detect temperature gradients within the soil surface.
4. Noncontact electromagnetic sensors to measure soil moisture [23].
5. An optical or infrared camera to provide images that can be overlaid over the radar hologram.

Additional location systems are under development, but not yet integrated in the prototype:

- Optical systems for absolute positioning of the radar head for use in indoors or in an environment in the presence of EMI restrictions. These would supplement the robot's position detected by the encoder.
- High-accuracy GPS Sensors for use in open areas.

The surface relief effects due to the air gap can be compensated by adding a phase term into the reconstruction algorithm of the holographic image. The problem here is the accuracy of the measurement of the air gap with ultrasonic methods because the wavelength in air dictated by the range resolution for the phase compensation (a few mm) becomes comparable with irregularities of the soil surface (stones, holes, etc.). In order to mitigate this problem, an arrangement of two cross hemi-cylindrical sensors operating at 100 kHz with real-time acquisition and a ranging algorithm has been developed [22].

10.5 Examples of Real-Time High-Resolution Holographic Imaging with Robotic and Automatic Scanners

10.5.1 High-Resolution Imaging for Rapid Investigation *in situ* of Structures Made of Dielectric Materials

The initial experiment tested the scanner's ability to obtain a high-resolution image by scanning two metal letters "W and I" with a total expanse of 210 mm and height 110 mm. These two letters were fixed on the bottom of the plain wooden table in Figure 10.6 with 30 mm thickness. The two letters were placed close to the central longitudinal iron bar of the table that has a dimension of 20 mm along y-axis.

The robotic scanner was set to scan at 5 frequencies, 3.6, 3.7, 3.8, 3.9, and 4.0 GHz, over a length of 380 mm along the x direction. Spatial sampling along both the x and y directions was 5 mm. The robotic scanner moved along the x direction, which corresponds to the cross-polar receiver channel, while the direction y corresponds to the parallel receiver. Assuming a relative permittivity of the wooden plank of 5, the corresponding wavelength at 4 GHz is $\lambda_{\text{wood}} = c/f\sqrt{5} = 3 \times 10^8/(4 \times 10^9 \sqrt{5}) = 33.5$ mm.

Figure 10.7 compares the optical scan of the two metal letters "W I" with the radar image at the frequency of 3.6 GHz. The image was obtained in real time and the total time for the experiment was about 3 minutes.

The interesting result is that the obtained detected image of the shape of the two letters had a resolution comparable with the expected theoretical one (see Table 10.1), namely: $\lambda_{\text{wood}}/4 = 33.5/4 = 8.3$ mm. The spatial coherence of the acquired data allows the reconstruction of the shape with only small distortion. In particular, the straight line of the metal bar is well reconstructed and a slight inclination of the robot trajectory with respect to the bar can be seen. Moreover, the possible subtle variations in dielectric due to the wood grain may have produced the small difference in the image reconstruction of the "W."

Finally, the beam divergence at the depth of 30 mm tends to enlarge the size of the object represented by the holographic image. For a more quantitative evaluation of the resolution, the software interface on the laptop PC provides a cross-hair for the generation of x–y section of the image. We selected the central image of Figure 10.7 because the cross-polar
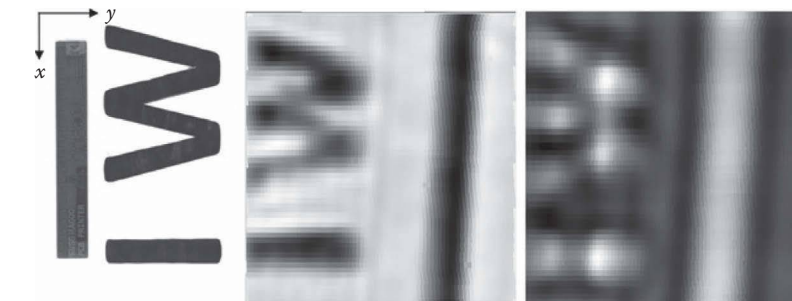
FIGURE 10.7
Comparative optical and radar scan. (Left) The optical scan of the metal letter glued on a paper sheet and a 20 cm ruler. (Center) Cross-polar channel at 3.6 GHz. (Right) Parallel channel at 3.7 GHz.
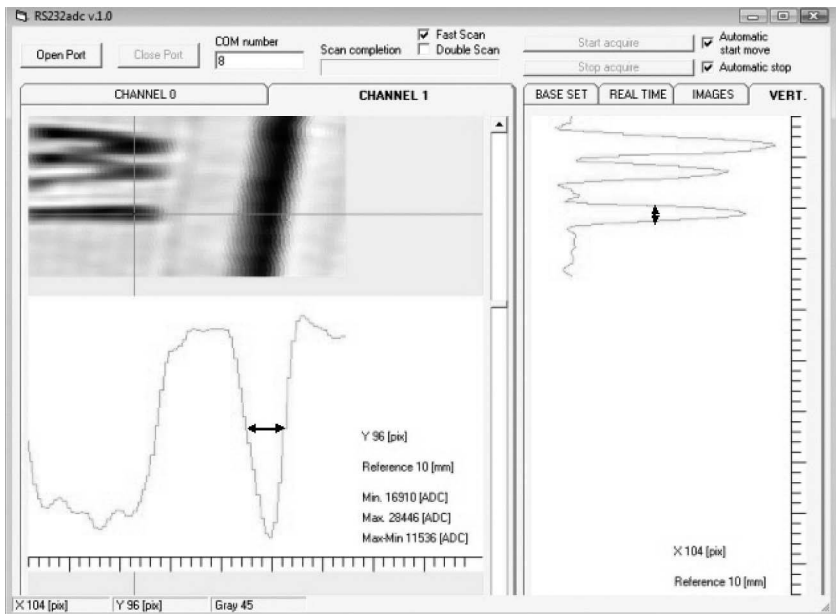
FIGURE 10.8
Evaluation of two targets width: "I" letter on the right and metal bar on the bottom left. The diagram reference is 10 mm.

channel provides a more accurate profile of the metal bar. In Figure 10.8, it is possible to estimate the width of the letter I and the metal bar: the -6 dB width of the metal bar is 32 mm and the width of the "I" is 19 mm against the real width of 21 mm. In both cases, the dimension has been estimated correctly within the theoretical resolution of the 4 GHz holographic radar. Such results are difficult to achieve with manual scanning since the operator would have to follow an ideal line with a deviation less than 8.3 mm. Even, if possible, for an expert operator in laboratory on a small area, it is very difficult to achieve this in the field when investigating area with dimensions in meters.

10.5.2 Outdoor Experiments for Landmine Detection

It is intended that the robotic scanner will find applications to surveys in critical/risky environments, such as the detection of minimum-metal antipersonnel landmines [5,10]. This application requires a high radar probability of detection and low rate of false alarms. The enhanced robotic platform positioning precision will enhance the performance. In such environments, one of the main issues will be the variability of soil characteristics (moisture content, grain size variations, surface roughness, etc.), and signal-processing strategies will play a key role in mitigating detrimental effects.

A demonstration of the developed system searched for inert landmines and clutter objects buried for several months at shallow depth in natural sandy soil in the outdoor test bed at the University of Florence in Italy. After several months, the originally flattened soil surface had roots and grass present at the edges of the area. The irregular surface had undulations up to 3 cm height as shown in Figure 10.9.

The buried objects in this outdoor test bed have already been described in a previous work [24], but in this experiment, their relative positions were found to have changed by natural settling of the sandy soil.

The robotic scanner was programmed for fast operation with two frequencies (3.6 GHz and 3.9 GHz) and spatial sampling on a 10 mm square grid. In order to limit cumulative errors, the scan length was limited to 650 mm with the overall image length of 1300 mm covered in two successive acquisitions of 650 mm each. The width covered by the lateral movement is 250 mm.

The real-time images obtained on the display of the remote laptop PC are shown in Figure 10.10 for the parallel and cross-polar channels at the two programmed frequencies. The total time to complete the experiment was about 18 minutes.

The results obtained and shown in Figure 10.10 indicate that the scanner has adequate spatial resolution to describe the circular shape of the iron disk and enough sensitivity to detect an empty plastic bottle. A circular plastic box with almost the same diameter as the iron disk, and buried close to it, is more difficult to detect because of the much lower dielectric contrast with respect to the sandy soil. Moreover, the surface irregularities at the edges of the iron disk generate additional noise that masks the reflection from the low reflectivity plastic box.

FIGURE 10.9
The robotic scanner searching the test bed of the University of Florence. Inert mines and clutter had been buried for several months before the test.
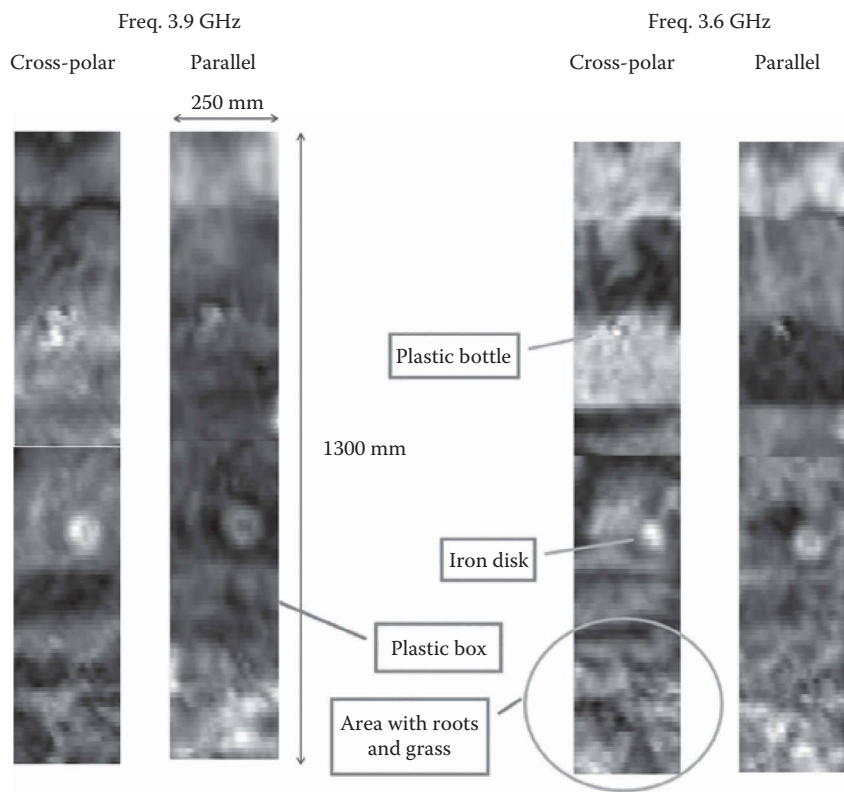
FIGURE 10.10
Results of scanning surrogate mines and clutter in the outdoor test bed.

Apart from possible improvements in the selection of the lower operating frequency of the radar (e.g., 2 GHz) for achieving better penetration and the full reconstruction of the hologram with I/Q signal components, the experiment demonstrated the ease and efficiency of high-resolution imaging using holographic radar even in an outdoor environment.

10.5.3 Nondestructive Test and Evaluation of Thermal Insulation for the Aerospace Industry

10.5.3.1 Objectives in Thermal Insulation Inspection

The Space Shuttle Columbia disaster of February 1, 2003 killed all seven crew members. Figures 10.11 and 10.12 show the launch and recovered debris laid out during the investigation. This and other incidents, which fortunately did not lead to such catastrophic consequences, have aroused interest in the development of new methods for nondestructive testing of insulation and thermal protection coatings on spacecraft and fuel tanks [25,26,27,28,29,30].

In the opinion of NASA investigators, one of the causes of the Columbia disaster was voids in the thermal protection coating on the shuttle's external fuel tank [31,32] as shown in Figures 10.13 and 10.14. The external tank contains liquid oxygen and hydrogen propellants stored at −183 and −253°C, respectively. To reduce fuel vaporization and prevent icing of tank surface that could fragment and damage the shuttle, the tank has an insulating
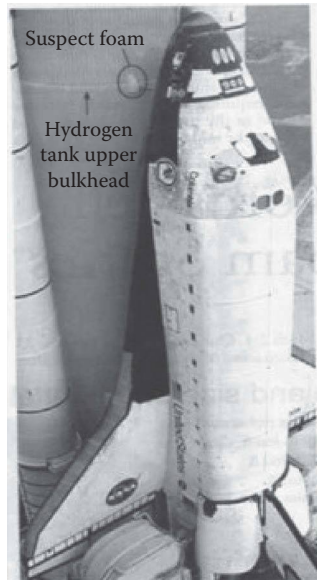
FIGURE 10.11
Space Shuttle *Columbia* take-off on January 16, 2003.

FIGURE 10.12
Result of *Columbia* disaster on February 1, 2003. Remains of the spaceship collected on the ground were laid-out in a hangar.

polyurethane foam coating [33]. The thickness of the foam is within the range of 25 mm to 50 mm [34]. If the super-cold external tank is not sufficiently insulated from the ambient warm and moist air, then atmospheric water vapor condenses inside the foam voids.

According to this hypothesis, during the launch of Columbia's 28th mission, water that had condensed inside voids rapidly vaporized (boiled) as a result of lowering pressure with increasing altitude following launch [32]. As a result of this explosive boiling, a piece of foam insulation broke off from the external tank and struck the left wing, damaging heat-protective leading edge panel. When Columbia reentered the atmosphere after the mission,

FIGURE 10.13
Space Shuttle Columbia on the launch pad. Yellow design elements are thermal insulation coating of the external cryogenic tank. (From *Aviation Week & Apace Technology*, 27–28, 2003.)
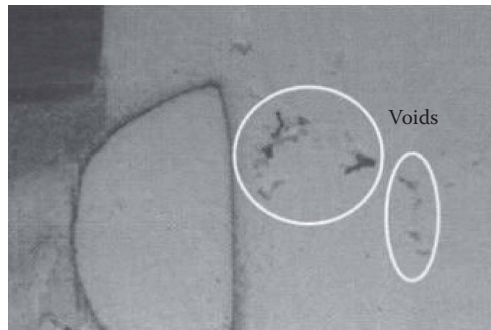
FIGURE 10.14
Cross section of thermal protection coating of shuttle external tank. Voids are visible inside of insulation polyurethane foam. (From *Aviation Week & Space Technology*, 31, 2003.)

this damage allowed plasma (produced ahead of the craft during its flight in stratosphere) to penetrate and destroy the wing structure, causing the spacecraft to break up as shown in Figure 10.12. Most previous shuttle launches had seen similar, but more minor, damage and foam shedding, but the risks were deemed acceptable as shown in Figure 10.15 [35].

It is well known that the tiled thermal protection coatings of return vehicles like the Space Shuttle are exposed to high mechanical, and especially thermal, influence on reentry. In fact, after the first flight of Columbia (April 12, 1981), 16 tiles were lost and 148 tiles were damaged [31]. Similar problems with more serious after-effects arose after the first and only flight of the Russian *Buran* on November 15, 1988. Postflight inspection showed partial destruction to complete loss of thermal shielding tiles as shown in Figure 10.16 [27]. Such damage could lead to a repeat of the *Columbia* disaster in future missions for similar spacecraft.

FIGURE 10.15
A torn off piece of the insulating foam falls along the surface of the external fuel tank. (From Report of Columbia Accident Investigation Board, 2003)

FIGURE 10.16
Destruction of the three tiles placed directly behind 21st section of the wing leading edge of the spacecraft *Buran*. (From *Aviation Week & Space Technology*, 31, 2003.)

Shedding of thermal insulation is connected with impurities and/or insufficient quality control in the bonding of foam or tiles to a space vehicle surface. Gluing tiles is carried out manually, and in these circumstances, it is difficult to maintain the necessary quality control. A variety of control methods are described in detail in [27], mainly involving destructive testing by "tearing off."

Widely applied ultrasonic diagnostic methods for nondestructive testing of different constructions [25] are insufficiently effective for foam insulation diagnostics due to polyurethane's high porosity, which leads to high levels of incoherent acoustic scattering and attenuation [36]. Similar considerations apply to the silicate fiber tiles that shield the outer surface of the Space Shuttle and *Buran*.

Microwave diagnostics using holographic subsurface radars [28,37] could become a good alternative to ultrasonic testing. The basic advantage of microwave diagnostics in comparison with ultrasonic ones is the fundamental difference in physical properties affecting the propagation of electromagnetic versus acoustic waves in heterogeneous media. Electromagnetic waves reflect from inhomogeneities only when their dielectric contrast is sufficient. Thus, electromagnetic waves propagate practically without loss in porous materials such as polyurethane foam insulation wherein the dielectric of air in pores almost matches that of the matrix foam [26]. Moreover, the pore dimensions are much smaller than the length of electromagnetic wave, so the foam can be considered as the continuous medium.

The thermal protection tiles received hydrophobization to prevent moisture penetration. New tiles are checked by immersing them in water for 24 hours followed by weighing [27]. However, this method is not suitable for testing of tiles already installed on the spacecraft, especially for critical postflight inspection. However, in this case, it is possible to use microwave methods. In particular, this example describes the use of holographic radar, which has a high sensitivity to the presence of moisture due to the high relative dielectric constant of water (approximately 80) relative to air or foam (approximately 1) [38].

10.5.3.2 Radar Inspection of a Thermal Protection Coating Sample

The test sample of thermal insulation with artificial flaws used polyurethane foam of 40 mm thickness glued on an aluminum alloy plate of 5 mm thickness. Design of the sample and positions of the flaws are shown in Figure 10.17. The sample form was chosen to mimic the actual construction of spacecraft fuel tank insulation coating.

The sample dimensions were 500 by 400 mm and made in two stages. On the first stage, the central circle, 270 mm in diameter, was sprayed with adhesive, but with three round cuts on the bottom surface of the foam. At the cuts, prime coating and glue are missing (usual total thickness = 200 microns). Instead, the inner surface of the cuts had the prime coating and glue. On the second stage, the rest of the sample was filled. This sample imitated defective gluing on the foam–metal contact.

10.5.3.3 Experimental Results

The experiment used the highest available frequency version of RASCAN-5 holographic radars, with an operating frequency of 15 GHz. The low attenuation factor of polyurethane foam for electromagnetic waves and the need for high resolution to detect small anomalies determined the frequency band choice. The dielectric permittivity of this material is essentially the same as for vacuum, that is about 1. According to data presented in [26], the complex permittivity of the foam sprayed on the external fuel tanks of the Space Shuttle is $\varepsilon = (1.05 - j0.003)$ and the density is only 4% of that for water. This is because the polyurethane foam consists mostly of pores filled by air. Laboratory experiments with RASCAN-5/15000 radar have shown that penetration depth in polyurethane foam is more than 16 cm, which with margin exceeds the Space Shuttle foam insulation thickness [34].

However, it should be noted that the properties of the bulk polyurethane material depend on the fabrication process, and may vary within wide limits, so the density of its industrial samples lay in the range of 48–287 kg/m^3 [36]. Polyurethane foam has the lowest heat conductivity among all modern materials. Depending on its density, polyurethane foam thermal conductivity varies in the range of 0.019–0.033 W/m·K. Due to these
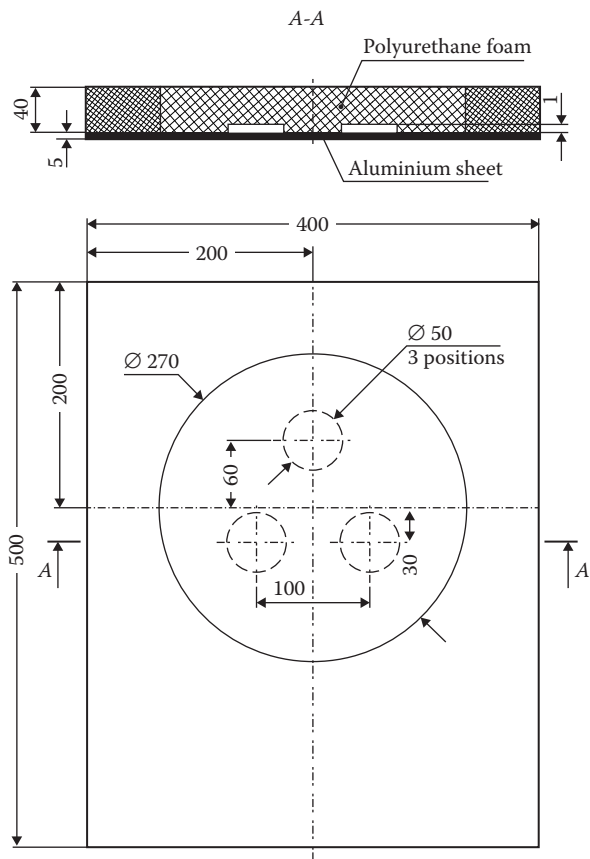
FIGURE 10.17

Sketch of the thermal coating sample showing the polyurethane foam coating and cut out regions mimicking the space craft fuel tank insulation.

characteristics, polyurethane foam is widely used as insulation material in various fields of industry, as well as military and space engineering.

Note that using frequencies around 15 GHz for diagnostics of other common structural materials is hardly possible because of the frequency-dependent attenuation of electromagnetic waves, that is generally a sharp increase in the absorption factor for frequencies above 10 GHz. Therefore, for diagnostics of building structures with concrete, wood, and plaster construction, it is more appropriate to use frequencies in the range of 1.5–7 GHz to obtain good results [38].

The experiments on thermal protection coatings used manual scanning of the sample surface as shown in Figure 10.18 [39]. It required about 4–5 min to scan the sample with dimensions of 40 by 50 cm as shown in Figure 10.17. The robotic scanner described earlier could have performed the inspection faster. The complex microwave hologram (real and imaginary components) and the digital reconstruction (1)–(3) for a signal frequency of 14.6 GHz are shown in Figure 10.19.

The procedure for hologram reconstruction using the algorithm described previously is very fast – requiring less than 1 second. One can readily see on these microwave images the three flaws, and the round sample border created by the two-stage production of the test sample.

FIGURE 10.18
Scanning of thermal insulation coating sample.

(a)　　　　　　　　　　　　　　　　(b)

(c)
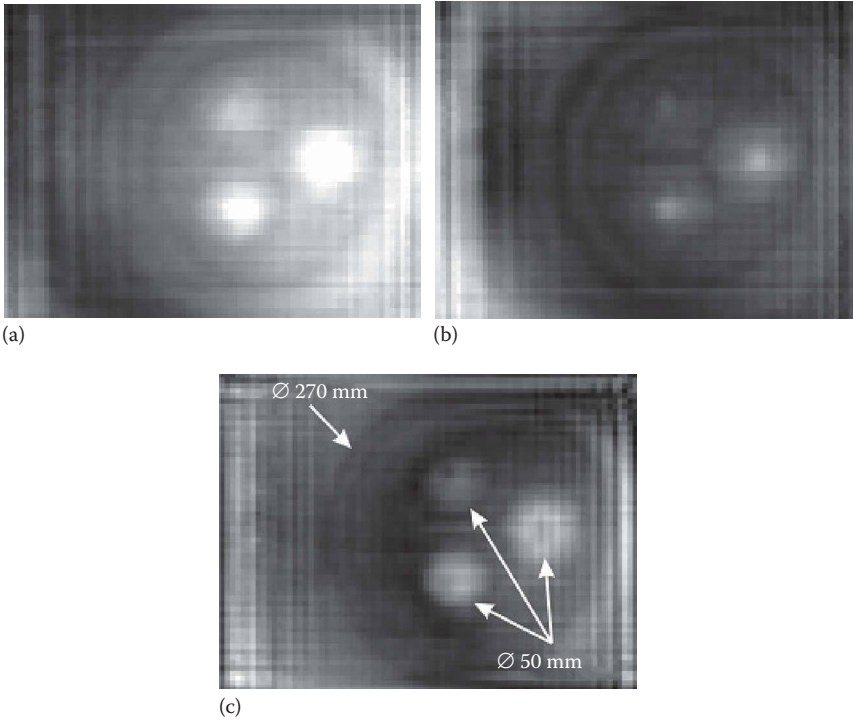
FIGURE 10.19
Result of the experiments in Figure 10.18: (a) real part of the hologram, (b) imaginary part of the hologram, and (c) the reconstructed image.

The vertical and horizontal stripes in Figure 10.19 are the result of the reflection of electromagnetic waves, emitted by the radar in the medium, from the end faces of the sample insulation, primarily from the border of the underlying aluminum plate, that is they are edge effects. Cyclical variation with distance in the reflected wave phase combined with the constant phase of the reference signal forms a striped pattern. This phenomenon is essentially the "zebra effect" that was described and explained in [40].

The examination of heat protection coatings and thermal insulation of space vehicles glued to a metal fuselage is a specialized task for radar system. This is because the metal surface is a perfect mirror for microwaves. The specular reflection ensures certain specificity in the process of hologram reconstruction and requires that this be accounted for when interpreting the results.

An experiment demonstrating the processes occurring in a microwave-transparent material (polyurethane foam) above a perfectly reflective metal surface used the configuration of Figure 10.20. Metal spokes inserted through the side of a sample are labeled on the left of this figure as 1 and 2. Spoke 1 was inserted parallel with the metal surface at a depth of 13 cm (distance above the metal surface of 2.3 cm). The second spoke was inserted in the polyurethane foam at an average depth of 13.5 cm but with a slight dip relative to the surface to demonstrate the above-mentioned "zebra effect" [40].

To determine the true depth of the objects inside the foam, it was necessary to take into account the 3 mm Plexiglas sheet that covers the scanning surface for improving the sliding of the radar head. Another important effect is related to the presence of the metal plate that underlies the polyurethane foam and reflects the microwave as an ideal mirror. The same as in optics, the mirror reflection of spokes must be observed behind the plate.

Upon reconstruction of the microwave holograms from the interference pattern recorded by the radar, the image is focused at a distance specified by the parameter z (1)–(3). The distance, at which the operator-determined "best focusing" for a target occurs, is presumed to be its real depth, $z = z_0$. Results of microwave hologram reconstruction for different depths in the experiments with the spokes are shown in Figure 10.21.

In Figure 10.21, the two top images correspond to the original complex holographic interference pattern recorded in two radar signal components; real and imaginary. Images below correspond to successively deeper hologram reconstructions: where depth $z = 0$, 2.7, 4.7, and 6.7 cm, respectively. Depth 2.7 cm corresponds approximately to the depth of
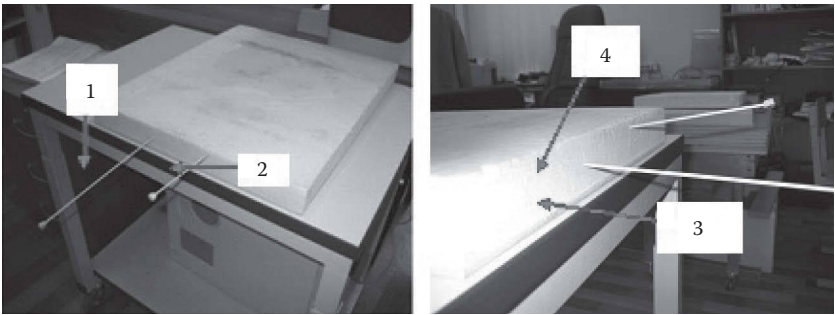
FIGURE 10.20
An experiment demonstrating the processes occurring in a microwave-transparent material (polyurethane foam) above a perfectly reflective metal surface. The radar scanned for metal spokes embedded into the foam covering of the sample: (1) spoke 1, (2) spoke 2, (3) a 5-mm aluminum alloy plate, and (4) a 40-mm-thick polyurethane foam layer.
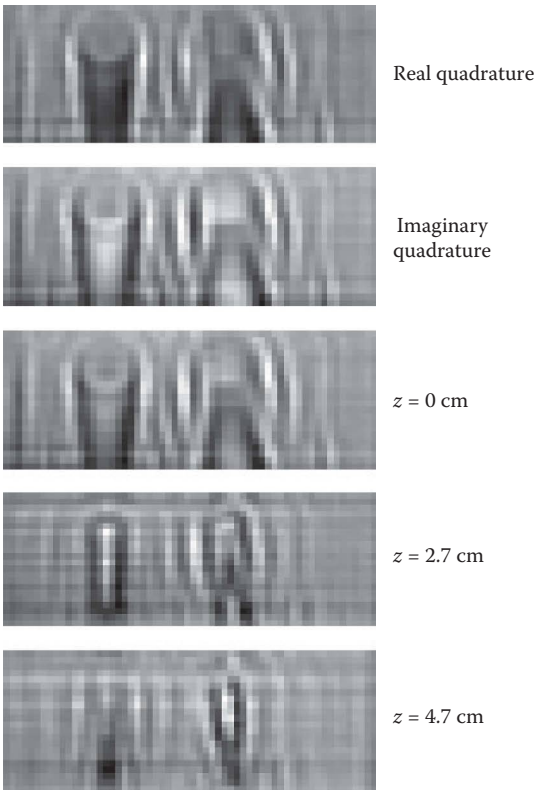
FIGURE 10.21
The results of experiments with spokes inserted into foam as shown in Figure 10.20. The original complex holographic interference pattern (real and imaginary) is at the top, with successively deeper hologram reconstructions below. Depth 2.7 cm corresponds approximately to the depth of the object, 4.7 cm is the position of the underlying metal surface, and 6.7 cm is a virtual image that corresponds to a mirror reflection of the spokes from surface of the metal surface.

the object, 4.7 cm is the position of the metal surface, and 6.7 cm is a virtual image that corresponds to mirror reflection of the spokes from surface of the metal plate.

It is necessary to note that the contrast of the virtual image of spoke 1 at 6.7 cm with respect to the background has changed to the opposite sign in comparison with the real image of the object at a depth of 2.7 cm. This effect is associated with the phase inversion of the electromagnetic wave by 180° upon its reflection from the surface of the metal [41], leading to the polarity reversal in the virtual image contrast pattern. Such complexities indicate needed further investigation to understand the details of microwave holograms recorded in dielectric media located above a metal surface.

Diagnosis of thermal insulation and heat protection coatings glued onto a metal surface is a very specialized task since the metal surface fully reflects the electromagnetic waves. For impulse radars, such targets are characterized by multiple reflections of signal between radar antenna and metal substrate, which obscure the desired target in the recorded impulse radar images. Although holographic radar is free from this shortcoming, the presence of a perfectly specular reflective metal substrate beneath desired targets must be considered when interpreting the results of holographic imaging.

These experiments showed that the proposed diagnostic method for thermal insulation using holographic subsurface radars allows detection of internal defects within the coating. However, in the microwave images, the detected defects are subtle due to the low permittivity contrast between the defects and surrounding polyurethane.

It is possible that by increasing the operating frequency up to 24–25 GHz could enhance the radar sensitivity. This possibility is suggested by experiments with a lower frequency Rascan-5/7000 radar frequencies in range of (6.4–6.8 GHz), which did not detect the defects in the sample used for these experiments. This suggests that increasing the radar operating frequency should enhance both spatial resolution and sensitivity, probably with little loss of penetration due to negligible loss in the low electrical conductivity and low-scattering insulating materials.

10.6 Conclusions

Holographic subsurface radars provide specific advantages and disadvantages relative to impulse radar. Advantages include the possibility for very high-resolution, high-sensitivity plan-view imaging in real time, with the additional possibility for near-real-time full hologram reconstruction and associated target depth determination. The principal disadvantage is the inability to apply time-varying gain to enhance reflections from deeper targets (since the radar is continuous wave). However, this disadvantage is not noticeable for very low electrical conductivity media such as foam, and dry wood or sand (or other earth materials).

In order to take full advantage of the possibility for very high-resolution imaging, the positioning of the radar scanning head requires high precision, achieved with the robotic scanner described above. In addition, it can completely scan large areas otherwise impractical and/or tedious (and expensive) for hand-scanning. Finally, the robotic platform design is compatible with additional sensors to measure independent physical properties of subsurface targets. This will allow better detection rates for targets that may be subtle given one specific property (e.g., permittivity), but more distinct on another (e.g., acoustic velocity), and provide the possibility to more positively identify subsurface radar targets (e.g., discriminating landmines from clutter to lower false alarm rates). The authors' current work is focused on multisensor scanning systems.

Finally, the continuous wave holographic radar provides the unique ability to image targets on or near highly reflective surfaces. An example of this is detection of flaws in the attachment of heat-protective tiles to a metal spacecraft body – a task hardly possible for impulse radars.

References

1. Daniels, D. J. (ed.), *Ground Penetrating Radar 2nd Edition*, Vol 1, IET, London, 2004.
2. Taylor, J.D. (ed.), *Ultrawideband Radar: Applications and Design*, CRC Press, Boca Raton, FL, 2012.
3. Ivashov, S.I., Capineri, L. and Bechtel, T.D., Holographic subsurface radar technology and applications, in Taylor, J.D. (ed.), *UWB Radar. Applications and Design,* CRC Press, Boca Raton, FL, 2012, pp. 421–444.

4. Capineri, L., Falorni, P., Borgioli, G., Bulletti, A., Valentini, S., Ivashov, S., Zhuravlev, A., Razevig, V., Vasiliev, I., Paradiso, M., Windsor, C. and Bechtel, T. Application of the RASCAN Holographic Radar to Cultural Heritage Inspections. *Archaeological Prospection*, Vol 16, 2009, pp. 218–230.

5. Ivashov, S.I., Razevig, V.V., Vasiliev, I.A., Zhuravlev, A.V., Bechtel, T.D. and Capineri, L., Holographic Subsurface Radar of RASCAN Type: Development and Applications, *IEEE Journal of Selected Topics in Applied Earth Observations and Remote Sensing*, Vol 4, No 4, 2011, pp. 763–778.

6. Roberts, R., Corcoran, K. and Schutz, A., Insulated concrete form void detection using ground penetrating radar. *Structural faults and repair conference*. Edinburgh, Scotland, UK. 2010.

7. Pasternak, M., Miluski, W., Czarnecki, W. and Pietrasinski, J., An optoelectronic-inertial system for handheld GPR positioning, *15th International Radar Symposium (IRS),* 2014, pp. 1–4.

8. Trela, C., Kind, T. and Schubert, M., Positioning accuracy of an automatic scanning system for GPR measurements on concrete structures, *14th International Conference on Ground Penetrating Radar (GPR)*, 2012, pp. 305–309.

9. Falorni, P. and Capineri L., "Optical method for the positioning of measurement points", accepted to the *International Workshop on Advanced Ground Penetrating Radar (IWAGPR) 2015*, Florence, July 7–10, 2015, in print.

10. Arezzini, I., Calzolai, M., Lombardi, L., Capineri, L. and Kansal, Y., Remotely controllable robotic system to detect shallow buried objects with high efficiency by using an holographic 4 GHz radar, *PIERS Proceedings*, 1207–1211, March 27–30, Kuala Lumpur, Malaysia, 2012.

11. Capineri, L., Arezzini, I., Calzolai, M., Windsor, C.G., Inagaki, M., Bechtel, T.D. and Ivashov S. I., High resolution imaging with a holographic radar mounted on a robotic scanner, *PIERS Proceedings*, pp. 1583–1585, August 12–15, Stockholm, 2013.

12. Capineri, L., Razevig, V., Ivashov, S., Zandonai, F., Windsor, C., Inagaki, M. and Bechtel, T. RASCAN holographic radar for detecting and characterizing dinosaur tracks, *7th International Workshop on Advanced Ground Penetrating Radar (IWAGPR)*, 2013, pp. 1–6.

13. Razevig, V., Ivashov, S., Vasiliev, I. and Zhuravlev, A., Comparison of Different Methods for Reconstruction of Microwave Holograms Recorded by the Subsurface Radar, *Proceedings of the 14th International Conference on GPR*, June 4–8, Shanghai, China, 2012, pp. 335–339.

14. Finkelstein M.I., Subsurface radar: principal problems of development and practical use, *Proceedings of the 11th Annual International Geoscience and Remote Sensing Symposium,* Espoo, Finland, June 3–6, 1991, Vol 4, pp. 2145–2147.

15. Chapursky, V.V., Ivashov, S.I., Razevig, V.V., Sheyko, A.P., Vasilyev, I.A., Pomozov, V.V., Semeikin, N.P. and Desmond, D.J., Subsurface radar examination of an airstrip, *Proceedings of the 2002 IEEE Conference on Ultra Wideband Systems and Technologies, UWBST'2002*, May 20–23, 2002, Baltimore, MD, pp. 181–186.

16. Iizuka, K. and Freundorfer, A.P., Detection of nonmetallic buried objects by a step frequency radar, *Proceedings of the IEEE*, Vol 71, No 2, February 1983, pp. 276–279.

17. Junkin, G. and Anderson, A.P., Limitations in microwave holographic synthetic aperture imaging over a lossy half-space, *Radar and Signal Processing, IEEE Proceedings F*, Vol 135, No 4, August 1988, pp. 321–329.

18. Zhuravlev, A.V., Ivashov, S.I., Razevig, V.V., Vasiliev, I.A., Türk A.S. and Kizilay, A., Holographic microwave imaging radar for applications in civil engineering, *Proceedings of the IET International Radar Conference*, April 14–16, 2013, Xian, China. pp. 14–16.

19. Remote Sensing Laboratory, Nondestructive Testing Devices, RASCAN-4/4000 radar (4 GHz), http://www.rslab.ru/english/product/rascan4/result/animation.

20. Gabor. D., A new microscopic principle, *Nature,* Vol. 161, 1948, pp. 777–778.

21. Razevig, V.V., Ivashov, S.I., Vasiliev, I.A., Zhuravlev, A.V., Bechtel, T., and Capineri, L., Advantages and restrictions of holographic subsurface radars. Experimental evaluation, *Proceedings of the XIII International Conference on Ground Penetrating Radar,* Lecce, Italy, June 21–25, 2010, pp. 657–662.

22. Cambini, C., Giuseppi, L., Calzolai, M., Giannelli, P. and Capineri, L., Multichannel airborne ultrasonic ranging system based on the Piccolo C2000 MCU, *Embedded Design in Education and Research Conference (EDERC) 2014,* Milano, Italy, September 11–12, 2014, pp. 80–84.

23. Olmi, R., Priori, S., Capitani, D., Proietti, N., Capineri, L., Falorni, P., Negrotti, R. and Riminesi, C., Innovative techniques for sub-surface investigations, *Materials Evaluation*, Vol 69, No 1, pp. 89–96, 2011.

24. Borgioli, G., Bulletti, A., Calzolai, M. and Capineri, L., Detection of the vibration characteristics of buried objects using a sensorized prodder device. *IEEE Trans. Geoscience and Remote Sensing*, Vol 52, No 6, June 2014, pp. 3440–3452.

25. Capineri, L., Bulletti, A., Calzolai, M., and Francesconi, D., Lamb wave ultrasonic system for active mode damage detection in composite materials, *Chemical Engineering Transactions*, Vol 33, 2013, pp. 577–582.

26. Kharkovsky, S. and Zoughi, R., Microwave and millimeter wave nondestructive testing and evaluation, *IEEE Instrumentation & Measurement Magazine*, April 2007, pp. 26–38.

27. Gofin, M.Ya., *Heat resisting and thermal protecting systems of reusable space ships*. Moscow Aviation Institute, 2003. 672 p. (in Russian).

28. Ivashov, S.I., Vasiliev, I.A., Bechtel, T.D. and Snapp, C., Comparison between impulse and holographic subsurface radar for NDT of space vehicle structural materials, *Progress in Electromagnetics Research Symposium 2007*, Beijing, China, March 26–30, 2007, pp. 1816–1819.

29. Ivashov, S., Razevig, V., Vasiliev, I., Bechtel, T. and Capineri, L., Holographic subsurface radar for diagnostics of cryogenic fuel tank thermal insulation of space vehicles, *NDT & E International*, Vol 69, January 2015, pp. 48–54.

30. Ivashov, S., Razevig,V., Vasiliev, I., Zhuravlev, A., Bechtel, T. and Capineri, L., Non-destructive testing of rocket fuel tank thermal insulation by holographic radar, *Proceedings of the 6th International Symposium on NDT in Aerospace*, Madrid, Spain, November 12–14, 2014.

31. Report of Columbia Accident Investigation Board, 2003.

32. *Aviation Week & Space Technology*. April 7, 2003, p. 31.

33. *Aviation Week & Space Technology*. February 17, 2003, p. 27, 28.

34. *Aviation Week & Space Technology*. October 4, 2004, p. 58.

35. *Aviation Week & Space Technology*. August 1, 2005, cover page.

36. Dombrow, B.A., *Polyurethanes*, Reinhold Publishing Corporation, New York, 1957.

37. Lu, T., Snapp, C., Chao, T.-H., Thakoor, A., Bechtel, T., Ivashov, S. and Vasiliev, I., Evaluation of holographic subsurface radar for NDE of space shuttle thermal protection tiles, *Sensors and Systems for Space Applications. Proceedings of SPIE*, Volume 6555, 2007.

38. Ivashov, S.I., Razevig, V.V., Vasiliev, I.A., Zhuravlev, A.V., Bechtel, T.D., and Capineri, L., Holographic Subsurface Radar of RASCAN Type: Development and Applications, *IEEE Journal of Selected Topics in Earth Observations and Remote Sensing*, Vol 4, No 4, December 2011. pp. 763–778.

39. Gofin, M.Ya., BURAN Orbital Spaceship Airframe Creation: The Heat Protection Structure of the Reusable Orbital Spaceship, http://www.rslab.ru/downloads/scan.avi.

40. Inagaki, M., Windsor, C.G., Bechtel, T.D., Bechtel, E., Ivashov, S.I. and Zhuravlev, A.V., Three-dimensional views of buried objects from holographic radar imaging, *Proceedings of the Progress in Electromagnetics Research Symposium, PIERS 2009*, Moscow, Russia, August 18–21, August 2009, pp. 290–293.

41. Born, M. and Wolf, E., *Principles of Optics: Electromagnetic Theory of Propagation, Interference, and Diffraction of Light*, Cambridge University Press, UK, 1959.